

Supporting Information

for

Deciphering dynamic solid-liquid interphase for energetic high-mass-loading energy storage

Jinxin Wang[‡], Wei Guo^{‡*}, Mingming Sun, Geng Zhang, Yang Meng, and Qiuyu Zhang*

Key Laboratory of Special Functional and Smart Polymer Materials of Ministry of Industry and Information Technology

School of Chemistry and Chemical Engineering

Northwestern Polytechnical University

Xi'an 710129, P. R. China

E-mail: weigu-nwpu@nwpu.edu.cn (W. Guo); qyzhang@nwpu.edu.cn (Q. Zhang)

[‡] These authors contributed equally to this work.

Experimental Section

Synthesis of MnOOH nanowires.

Firstly, MnOOH nanorods dispersion was generated by a typical hydrothermal process reported before.¹ 85 mg KMnO_4 and 42 mg polyvinylpyrrolidone (PVP, K30) were dissolved into 80 mL deionized water with continuous stirring. Then the solution was transferred into a 100 mL Teflon-lined stainless-steel autoclave and placed in an oven at 140°C for 25 h. After cooling down to room temperature, the uniform yellow MnOOH nanowires dispersion was generated. The MnOOH film (60 mg) was obtained by vacuum filtration of 100 mL MnOOH dispersion and washed with deionized water and ethanol several times, and then dried naturally.

Fabrication of P-Mn₃O₄@C electrode.

The MnOOH film (100 mg) and 900 mg $\text{NaH}_2\text{PO}_2 \cdot \text{H}_2\text{O}$ were placed in two quartz boats at the downstream and upstream regions, respectively. Then, a heat treatment at 400°C for 2 h with a ramp rate of 2°C min⁻¹ under medium flow rate Ar atmosphere was carried out to generate P-Mn₃O₄ film. And the EG dispersion (1.5 mg mL⁻¹) was obtained by a typical electrochemical exfoliation method as reported before.² The generated P-Mn₃O₄ film was uniformly dispersed in deionized water with a concentration of 0.5 mg mL⁻¹ through ultrasonic treatment. After that, tris(hydroxymethyl)aminomethane was dissolved in the mixed dispersion at a concentration of 2 mg mL⁻¹ under continuous stirring for 10 min. Subsequently, dopamine hydrochloride was also dissolved in the mixed dispersion at a concentration of 2 mg mL⁻¹ under continuous stirring for 5 min. The EG dispersion was then added to the mixed dispersion under continuous stirring for 40s, with a mass ratio of 1:4 between EG and P-Mn₃O₄. After that, the P-Mn₃O₄@PDA-5min/EG film was obtained by vacuum filtration of the mixed dispersion, washed with deionized water, and dried naturally. Ultimately, the P-Mn₃O₄@C-5min electrode was fabricated through heat treatment of P-Mn₃O₄@PDA-5min/EG film at 400°C for 2 h with a ramp rate of 2°C min⁻¹ under medium flow rate Ar atmosphere. By regulating the reaction time after dopamine hydrochloride, P-Mn₃O₄@C-0/2/10/20min electrodes were fabricated.

Preparation of Rec-Mg-MnO₂.

The Rec-Mg-MnO₂ electrode was fabricated by electrochemical activation with the prepared P-Mn₃O₄-C, a Pt-sheet electrode (20×20×0.1 mm³), and an Ag/AgCl electrode as the working electrode, the counter electrode, and the reference electrode, respectively. The electrochemical activation was carried out by using the CV method at 10 mV s⁻¹ in 1 M Mg(NO₃)₂ aqueous electrolyte, yielding the Rec-Mg-MnO₂ electrode *in situ*. For comparison, the activation was also performed in a series of electrolytes (2 M LiNO₃, 2 M NaNO₃, 2 M KNO₃, 1 M Ca(NO₃)₂, 1 M Zn(NO₃)₂), resulting in the Rec-Li-MnO₂, Rec-Na-MnO₂, Rec-K-MnO₂, Rec-Ca-MnO₂, Rec-Zn-MnO₂ electrodes, respectively. For preliminary assessment of electrochemical performance and reaction mechanism, electrodes with an active mass loading of approximately 6.4 mg cm⁻² were employed. Besides, a series of Rec-Mg-MnO₂-based electrodes with mass loadings of 5.1, 9.5, 19.5, 27.4 mg cm⁻² were fabricated to study high-mass-loading energy storage behaviors.

Materials characterization

The as-made materials were characterized by field emission SEM (FEI Verios G4), TEM and HR-TEM (FEI Talos F200X), XRD (Bruker, D8 Advance, Cu-K α , $\lambda=0.15406$ nm), Raman spectroscopy (HORIBA LabRAM HR Evolution), XPS (Kratos AXIS Ultra DLD), FTIR (Bruker Tensor27), and ICP-OES (Agilent 7800(MS)). X-ray absorption fine structure (XAFS) spectroscopy data was collected by the *RapidXAFS* 2M (Anhui Absorption Spectroscopy Analysis Instrument Co., Ltd.) with transmission (or fluorescence) mode at 10 kV and 20 mA, while the Si (440) spherically bent crystal analyzer (radius of curvature, 500 mm) was used for Mn.

Electrochemical characterization

The electrochemical performances of as-made Rec-Mg-MnO₂ and other electrodes were examined with a Corrtest electrochemical workstation (CS310) in a three-electrode cell in different cationic electrolyte (1 M Mg(NO₃)₂, 2 M LiNO₃, 2 M NaNO₃, 2 M KNO₃, 1 M Ca(NO₃)₂, 1 M Zn(NO₃)₂), with an Ag/AgCl electrode and a Pt sheet electrode (20 × 20 × 0.1 mm³) as the reference and counter electrode, respectively. The

specific capacitance (C_m , F g⁻¹) and areal capacitance (C_s , mF cm⁻²) were obtained based by the following equation:

$$C_m = (I\Delta t) / (m\Delta V) \quad (1)$$

$$C_s = (I\Delta t) / (S\Delta V) \quad (2)$$

Here, I , Δt , m , ΔV , S represent the discharge current (mA), the discharge time (s), the active mass of electrode (mg), the voltage range after an ohmic drop (V), and the effective area of electrodes (cm²), respectively.

Computation methods

The Vienna Ab Initio Package (VASP) was employed to perform all the density functional theory (DFT) calculations within the generalized gradient approximation (GGA) using the Perdew, Burke, and Enzerhof (PBE) formulation.³⁻⁵ The projected augmented wave (PAW) potentials were applied to describe the ionic cores and take valence electrons into account using a plane wave basis set with a kinetic energy cutoff of 500 eV.^{6, 7} Partial occupancies of the Kohn–Sham orbitals were allowed using the Gaussian smearing method with a width of 0.1 eV. The electronic energy was considered self-consistent when the energy change was smaller than 10⁻⁵ eV. A geometry optimization was considered convergent when the force change was smaller than 0.05 eV/Å. Grimme’s DFT-D3 methodology was used to describe the dispersion interactions.⁸ The vacuum spacing perpendicular to the plane of the structure is 25 Å. The dissociation energy is also calculated. The Brillouin zone integral utilized the surfaces structures of 2×2×1 monk horst pack K-point sampling. Then, the adsorption energies (E_{ads}) were calculated as $E_{\text{ads}} = E_{\text{ad/sub}} - E_{\text{ad}} - E_{\text{sub}}$, where $E_{\text{ad/sub}}$, E_{ad} , and E_{sub} are the total energies of the optimized adsorbate/substrate system, the adsorbate in the structure, and the clean substrate, respectively.

The removal energy was calculated using the equation: $G = E_{\text{ads}} + \text{ZPE} - \text{TS}$, where G , E_{ads} , ZPE and TS are the removal energy, total energy from DFT calculations, zero point energy and entropic contributions, respectively.

Finally, ion migration was calculated by the nudged elastic band (NEB) method.⁸ In the NEB method, the path between the reactant(s) and product(s) was discretized into

a series of five structural images. The intermediate images were relaxed until the perpendicular forces were smaller than 0.05 eV/\AA .

Supplementary Figures

Supplementary Note 1

We first carried out the optimization of the carbon coating on P-Mn₃O₄ by varying the polydopamine (PDA) coating time (Fig. S1). The electrochemical measurements in Na⁺ aqueous electrolyte demonstrate that Rec-Na-MnO₂ with a PDA coating time of 5 min presents the highest specific capacitance. It is noted that the carbon coating layer with the optimized thickness serves as the bifunctional “chainmail”, which not only finely enhances the structure stability *via* physical confinement and interfacial effect, but also facilitates the charge transfer by the continuous conductive network without suppressing the reactivity of Mn species.^{9, 10}

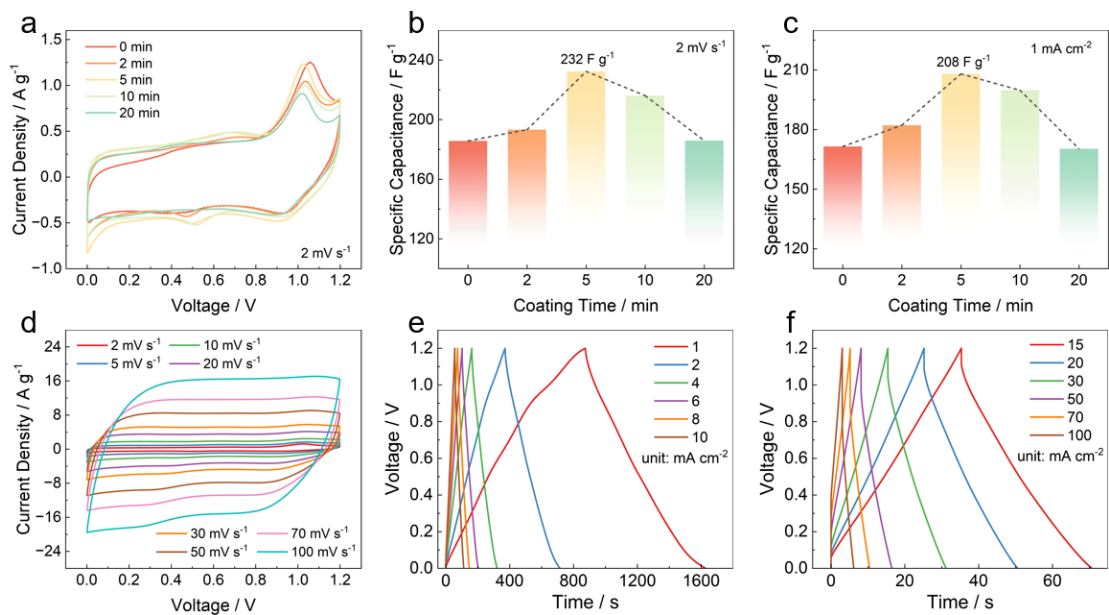


Figure S1. (a) CV curves of P-Mn₃O₄@C with different PDA coating times at 2 mV s⁻¹. (b-c) Specific capacitance of P-Mn₃O₄@C with different PDA coating times tested at (b) 2 mV s⁻¹ and (c) 1 mA cm⁻² in 1 M Na₂SO₄ electrolyte. (d) CV curves at different scan rates and (e-f) galvanostatic charge/discharge (GCD) profiles at different current densities of P-Mn₃O₄@C-5min.

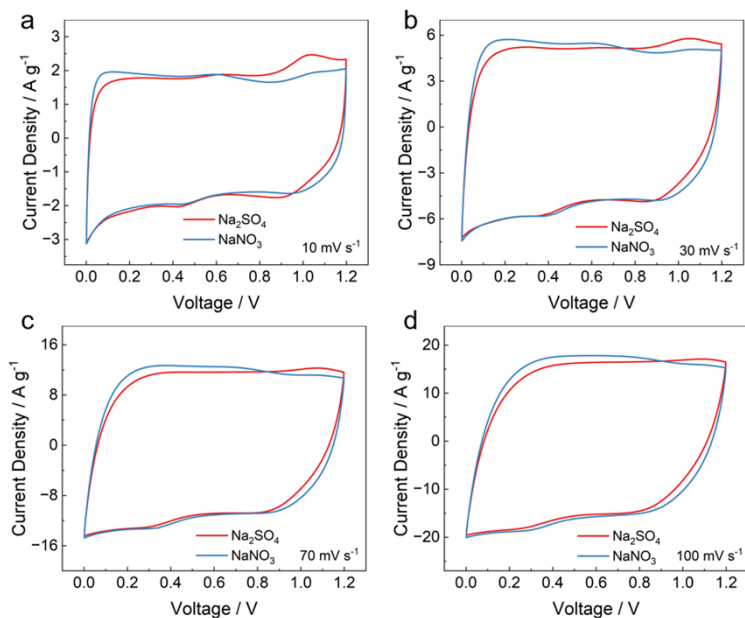


Figure S2. (a-d) Comparison of CV curves for P-Mn₃O₄@C-5min tested in 1 M Na₂SO₄ and 2 M NaNO₃ electrolyte at scan rates of (a) 10 mV s⁻¹, (b) 30 mV s⁻¹, (c) 70 mV s⁻¹ and (d) 100 mV s⁻¹.

Supplementary Note 2

It is noticed that the CV curves of Rec-Mg-MnO₂ show a well-maintained shape even at a high scan rate of 100 mV s⁻¹, indicative of a preferable rate performance (Fig. S3d). The capacitive contribution calculated by corresponding CV curves increases from 46% to 76% as the scan rate increased from 2 mV s⁻¹ to 30 mV s⁻¹ (Fig. S3e). Among these electrolytes, due to the abundant magnesium reserves in nature, aqueous Mg²⁺ storage holds great potential in scalable energy storage application, featuring high safety, competitive cost advantage, and environment-friendliness.¹¹⁻¹³

In addition, the response current density of the main oxidation peak can be fit with the following relationship

$$i=av^b \quad (3)$$

where i and v represent the response current and scan rate, respectively, while a and b are constants. The b value is utilized to identify capacitive control (b is near to 1) and diffusion control (b is near to 0.5), and b value of the main oxidation peak for Rec-Mg-MnO₂ is calculated to 0.82 (Fig. S3f). These indicate a combination of capacitive and ion-diffusion behaviour during the charge storage process.¹⁴

Note that the mass ratio of conductive filler EG is 25% in the 6.4 mg cm⁻² composite electrode, thus the 1.6 mg cm⁻² pure EG electrode was fabricated to understand its performance and capacitance contribution. As shown in Fig. S3g-h, the pure EG electrode delivers inferior areal capacitance of 53 mF cm⁻² at 2 mV s⁻¹ and 42 mF cm⁻² at 100 mV s⁻¹, in comparison to those of Rec-Mg-MnO₂ composite electrode (2725 mF cm⁻² at 2 mV s⁻¹, 1194 mF cm⁻² at 100 mV s⁻¹). The pure EG electrode only exhibits negligible integrated CV area (Fig. S3i) with a low capacitance contribution (less than 4%) at different scan rates (Figure S3j).

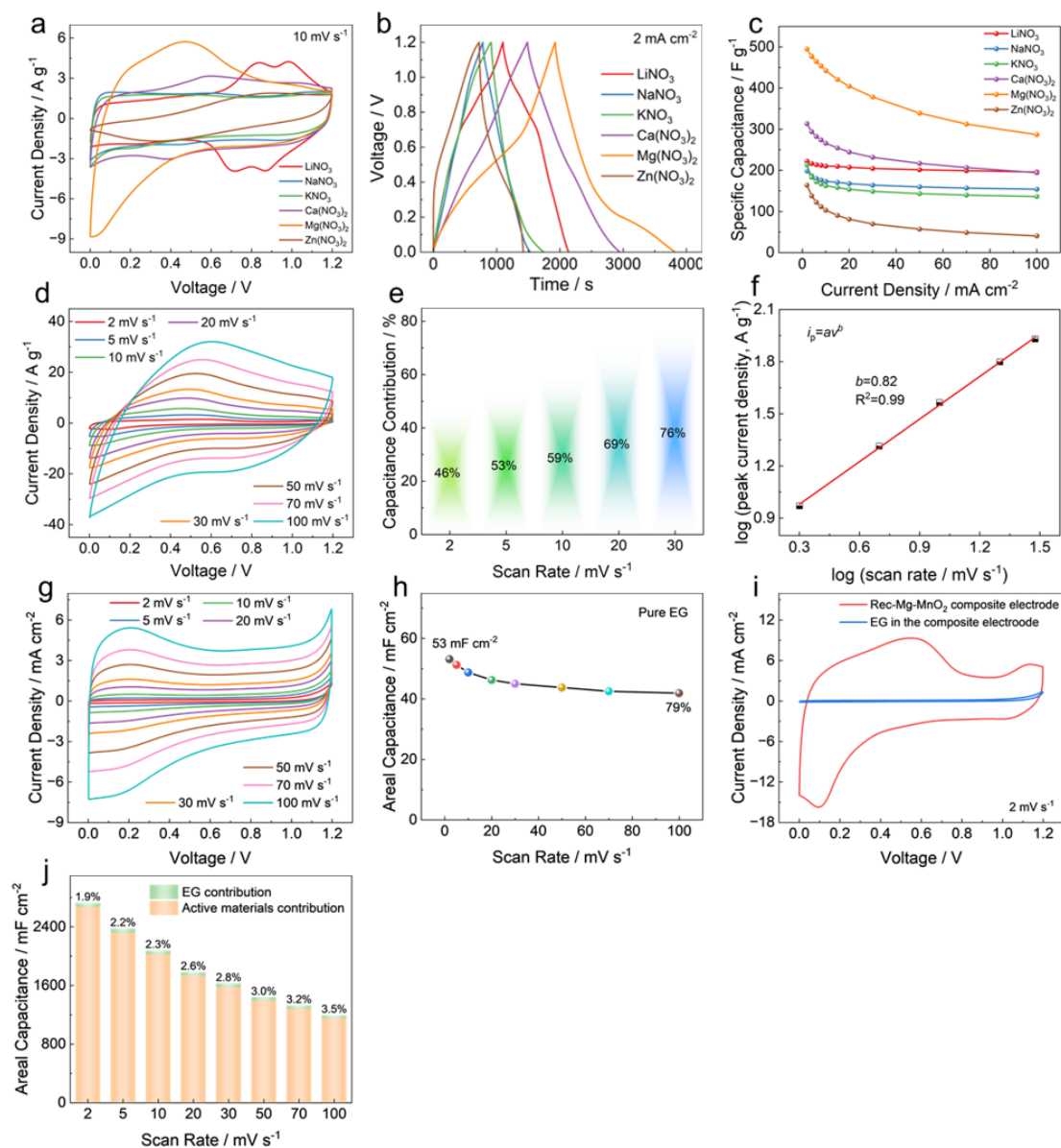


Figure S3. (a-c) Electrochemical performance for reconstructed electrodes in different cationic electrolytes. (a) CV curves at 10 mV s^{-1} . (b) GCD profiles at 2 mA cm^{-2} . (c) Specific capacitance at different current densities. (d) CV curves at different scan rates, (e) capacitive contributions, and (f) linear relationship between logarithm of the peak current density and logarithm of scan rate for the Rec-Mg-MnO₂. (g) CV curves, and (h) areal capacitances of the pure EG electrode at different scan rates. (i) A comparison of CV curves at 2 mV s^{-1} for the Rec-Mg-MnO₂ and pure EG electrodes. (j) Capacitance contribution percentages of EG in the composite electrode at different scan rates.

Supplementary Note 3

The electrochemical reaction dynamic was further evaluated by *operando* electrochemical impedance spectra (EIS) spectra. Fig. S4a exhibits that reduced semicircle diameter in the high-frequency region charge transfer resistance (R_{ct}) of the electrode reduces with cycling and tends to be stable after 20 cycles. In addition, the ion diffusion dynamic can be detected by the relaxation time constant (τ_0) and the Warburg factor (σ).^{15, 16} With the promotion of the activation process, τ_0 continues reducing until to the smallest value of 25.7 s after 30 cycles (Fig. S4b), while σ delivers a similar decreasing trend and subsequently stabilizes, indicative of the promoted ion diffusion rate (Fig. 1c). Based on the results above, though 30 cycles electro-activation, the Rec-Mg-MnO₂ electrode exhibited facilitated charge-transfer and ion-diffusion dynamics, responsible for the improved energy storage capability than other Rec-MnO₂ electrodes.

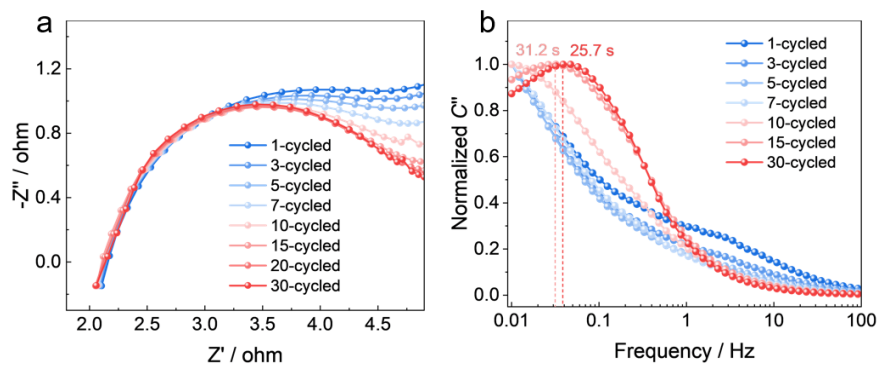


Figure S4. *Operando* EIS characterization of Rec-Mg-MnO₂ after different CV cycles. (a) Nyquist spectra. (b) Relationship between the normalized imaginary part capacitance (C'') and frequency.

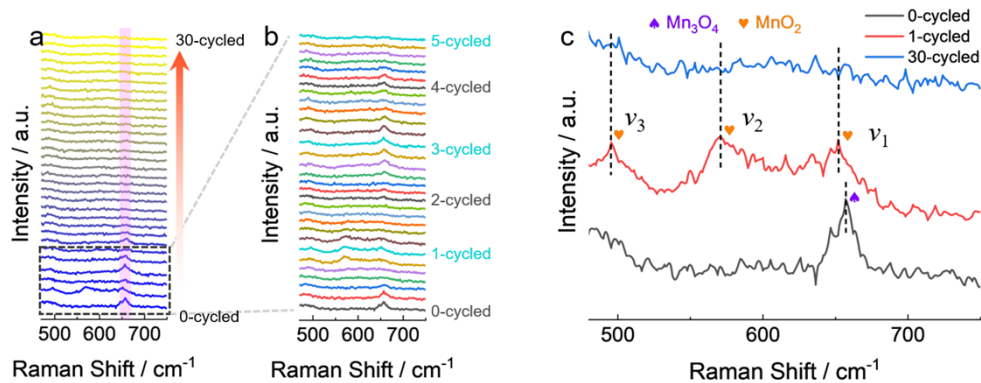


Figure S5. *Operando* Raman spectra for Rec-Mg-MnO₂ after different CV cycles.

Supplementary Note 4

The pristine P-Mn₃O₄@C demonstrates a rod-like morphology with a rough porous carbon layer surface (Fig. S6a) and features the characteristic XRD peaks (Fig. S7) corresponding to Mn₃O₄ (JCPDS card no. 24-0734). TEM images further display its rough rod-like morphology containing a carbon coating layer with an average thickness of ~4 nm (Fig. 1f and Fig. S6b), while the lattice spacing of 0.28 nm can be finely indexed to (211) planes of Mn₃O₄ (Fig. S6c). The corresponding TEM element mapping images display the uniform distribution of C, N, O, P, and Mn elements (Fig. S6d). Furthermore, generous disordered lattices are observed in P-Mn₃O₄@C-5min nanorods (Fig. S6c), which originates from P doping for the production of abundant defects to promote its reactivity.^{1,17}

Upon electrochemical cycling, few small nanosheets are generated on the surface of the nanorods, and the quantity and size of nanosheets gradually increase (Fig. S8), ultimately yielding the hollow core-shell heterostructure with the nanosheets uniformly distributed on the nanotubes due to Kirkendall effects, which depicts the formation of hollow structure in alloy reaction ascribed to the varied in-diffusion and out-diffusion rates of solid reagents (Fig. S9a and b).¹⁸ It is noted that the pillar effect of carbon layer can contribute to the high stability of the resulting structure. The 30-cycled sample, e.g., Rec-Mg-MnO₂@C, demonstrates the porous structure and numerous disordered lattice features (Fig. 1f, Fig. S9b and c), manifesting the generation of abundant mass-transport highways and active edge sites. As shown in *Ex-situ* XRD pattern (Fig. S7), with activation, the typical peaks of Mn₃O₄ decrease and disappear, while the peaks at 36.5, 60.3, 65.4° appear, indexed to the (11-1), (11-4), (020) planes of δ-MnO₂ (JCPDS card no. 43-1456), suggesting the phase transformation from Mn₃O₄ to the MnO₂, highly consistent with the *operando* Raman results. The lattice spacing of 0.25 nm can be indexed to (11-1) planes of δ-MnO₂ (Fig. S9c).¹⁹ The TEM elemental maps clearly display the homogeneous distribution of C, N, O, Mg, and Mn (Fig. S9d). For activation process into Rec-Na-MnO₂, similar morphological evolution results can be detected by *ex-situ* SEM images (Fig. S10). Whether in Mg(NO₃)₂, NaNO₃, or Na₂SO₄ electrolyte, P-Mn₃O₄@C undergoes the gradual reconstruction into δ-MnO₂ (Fig. S7).

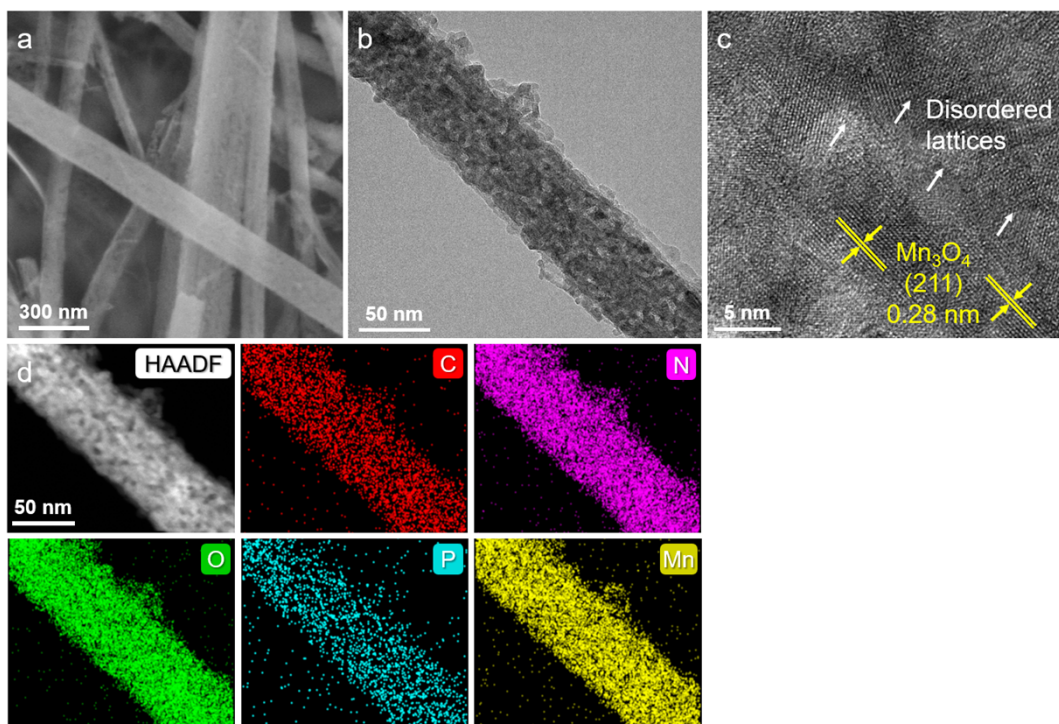


Figure S6. (a) SEM, (b) TEM, (c) high-resolution TEM images, and (d) the corresponding TEM elements mapping images of P-Mn₃O₄@C-5min.

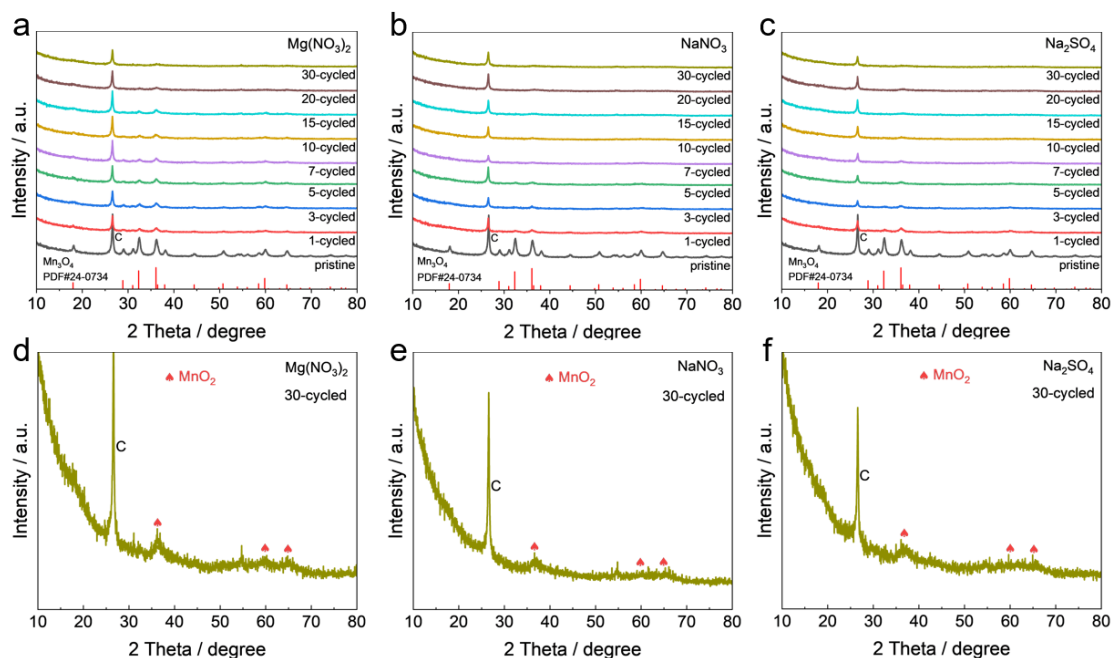


Figure S7. (a-c) *Ex-situ* XRD patterns of P-Mn₃O₄@C-5min before and after different CV cycles in (a, d) 1 M Mg(NO₃)₂, (b, e) 2 M NaNO₃, and (c, f) 1 M Na₂SO₄.

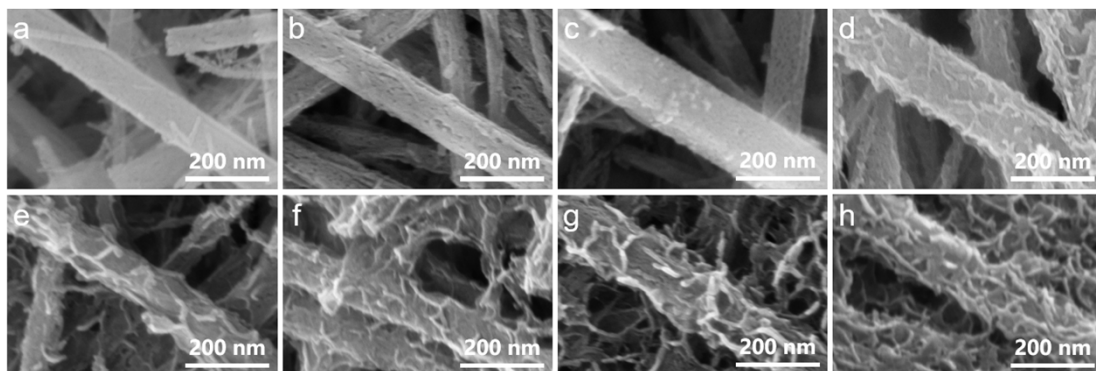


Figure S8. (a-h) *Ex-situ* SEM images of P-Mn₃O₄@C-5min after 1/3/5/7/10/15/20/30 CV cycles in 1 M Mg(NO₃)₂ electrolyte.

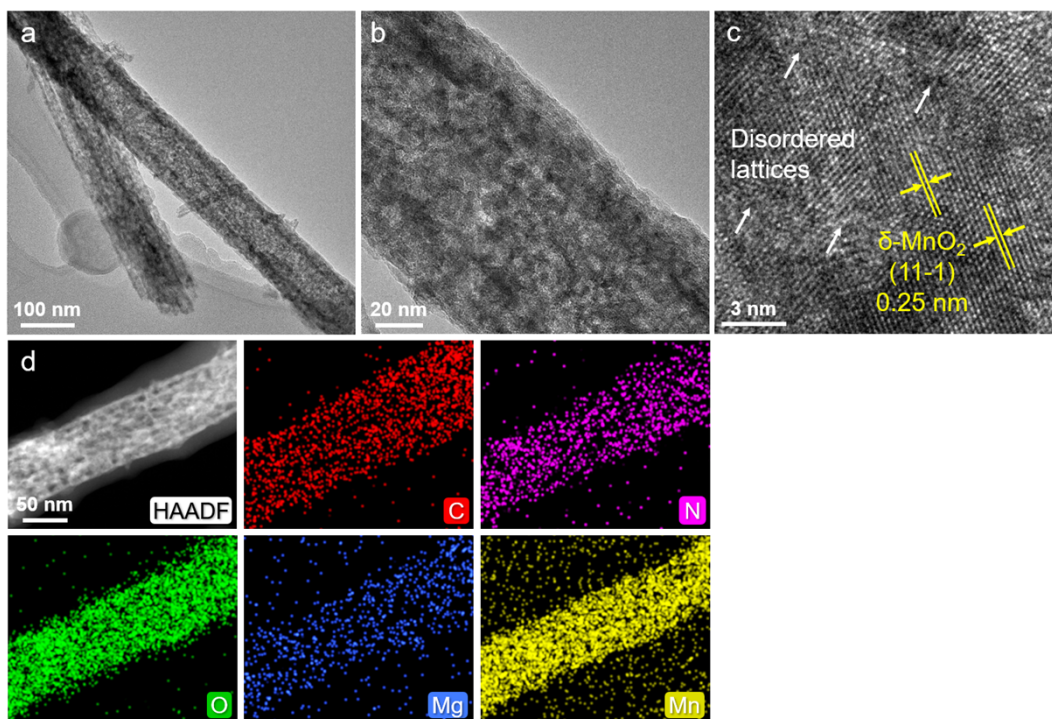


Figure S9. (a-b) TEM, (c) high-resolution TEM images, and the corresponding TEM elements mapping images of Rec-Mg-MnO₂.

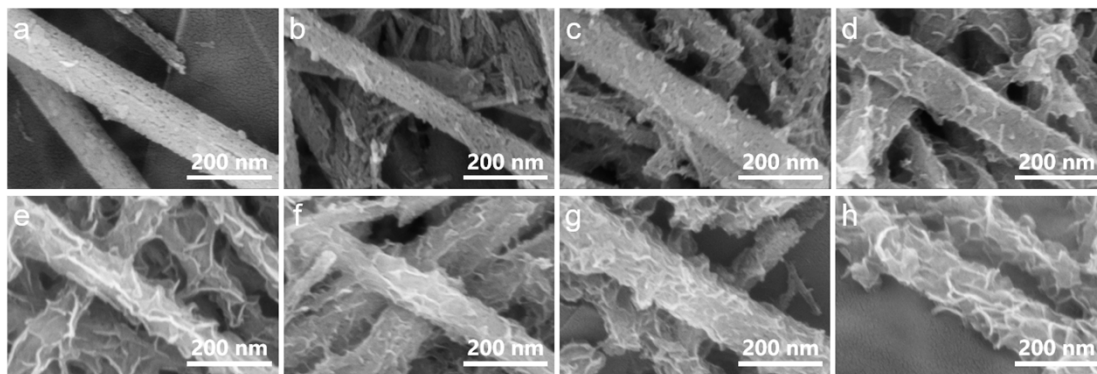


Figure S10. (a-h) *Ex-situ* SEM images of P-Mn₃O₄@C-5min after 1/3/5/7/10/15/20/30 CV cycles in 2 M NaNO₃ electrolyte.

Supplementary Note 5

The peak-energy differences (ΔE) of Mn 3s spectra decrease from 5.5 eV for a pristine sample to 4.8 eV for 30-cycled Rec-Mg-MnO₂, suggesting the oxidation of Mn average oxidation state from 2.8 to 3.7 (Fig. 1f and Fig. S11a).^{20, 21} This is also evidenced by the attenuation of the peak for Mn³⁺ (48.6 eV) and enhancement of the peak for Mn⁴⁺ (50.1 eV) for Mn 3p spectra, and a positive shift of Mn 2p_{3/2} (0.4 eV) for Mn 2p spectra, as the cycle numbers increases (Fig. S11b and c).^{22, 23} These XPS results are well in accordance with the transformation process from Mn₃O₄ into δ -MnO₂ in the TEM and Raman results. Interestingly, Rec-Na-MnO₂ shows the analogous process of increasing Mn valance state (Fig. S12a and b). The O 1s fine spectra (Fig. S11d) can be deconvoluted into three peaks situated at 530.1, 531.4, and 533.0 eV, assigned to M-O-M bond (O²⁻), M-OH bond (OH⁻), and H-O-H bond, respectively.²⁴ Besides, the peak of P-O bond (133.2 eV) gradually weakens, indicating the leaching out of P species during the reconstruction (Fig. S11e).^{25, 26} Moreover, the content of Mg elements is increasing progressively as the activation process continues according to the increased peak area of Mg 2s and Mg Auger, indicative of the increase in insertion amount of Mg²⁺ (Fig. 1e).²⁷

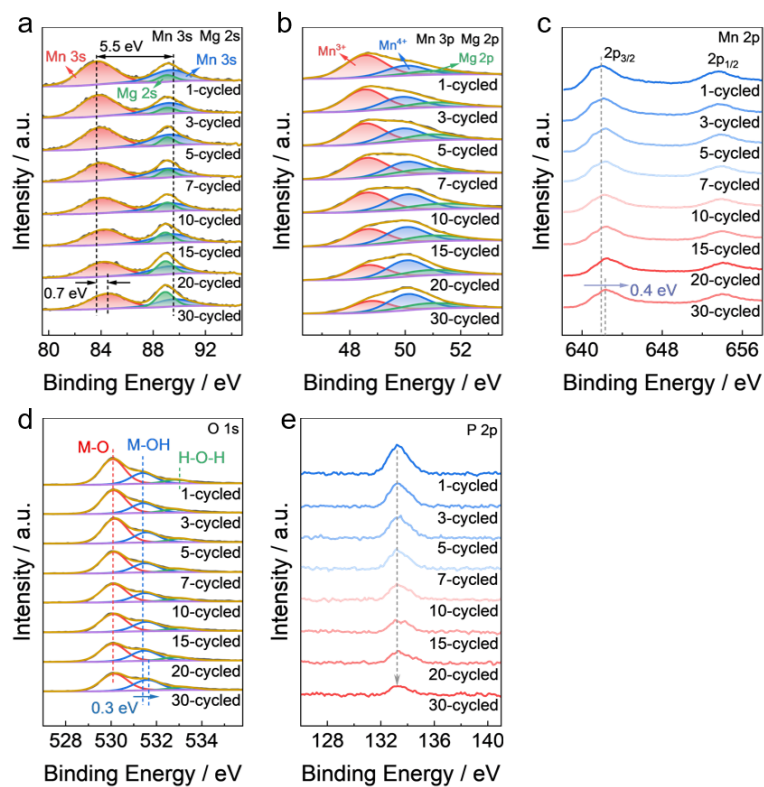


Figure S11. (a-e) *Ex-situ* XPS spectra of (a) Mn 3s and Mg 2s, (b) Mn 3p and Mg 2p, (c) Mn 2p, (d) O 1s, and (e) P 2p for Rec-Mg-MnO₂ after different CV cycles.

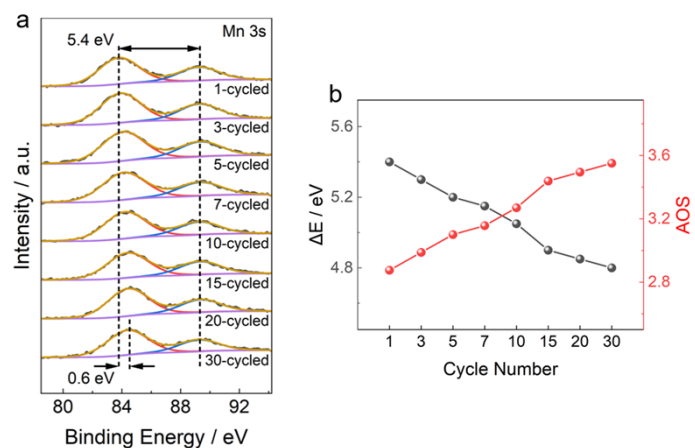


Figure S12. (a) *Ex-situ* XPS spectra of O 1s for Rec-Na-MnO₂ after different CV cycles. (b) ΔE value of Mn 3s peaks and AOS of Mn derived from Rec-Na-MnO₂ after different CV cycles.

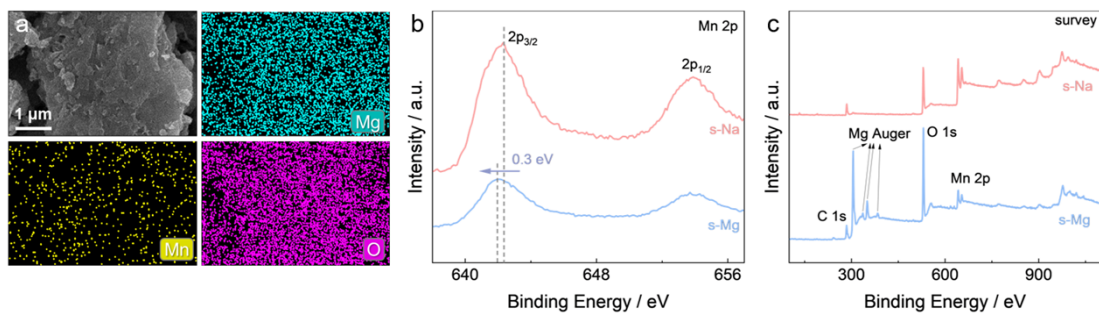


Figure S13. (a) SEM image and the corresponding mapping images of s-Mg. (b-c) XPS spectra of (b) Mn 2p and (c) full-spectra for s-Mg and s-Na.

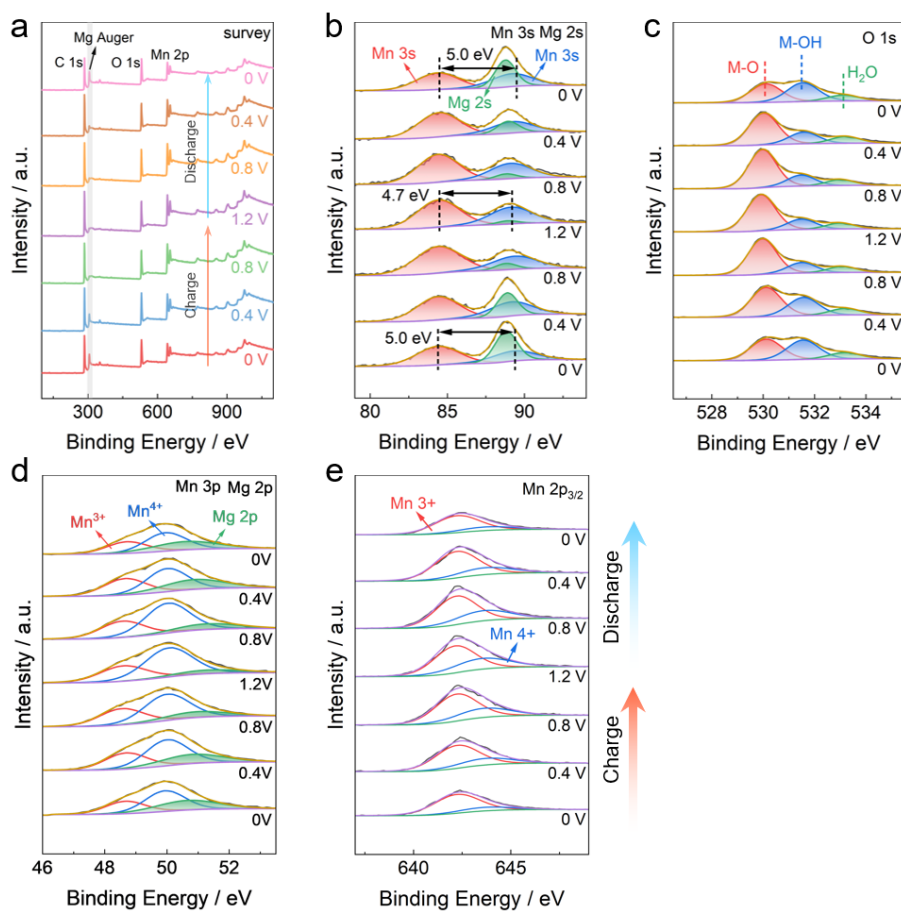


Figure S14. (a-e) *Ex-situ* XPS spectra of Rec-Mg-MnO₂ at different charged/discharged states. (a) full-spectra. (b) Mg 2s and Mn 3s. (c) O 1s. (d) Mn 3p and Mg 2p. (e) Mn 2p_{3/2}.

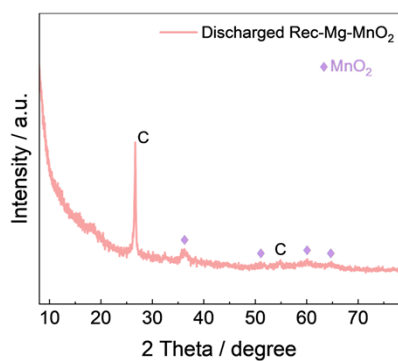


Figure S15. XRD spectra of Rec-Mg-MnO₂ at the discharged state.

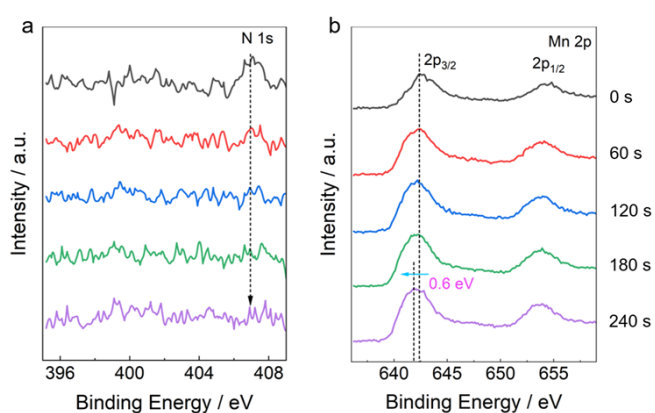


Figure S16. XPS depth spectra of (a) N 1s and (b) Mn 2p for Rec-Mg-MnO₂ at discharged state.

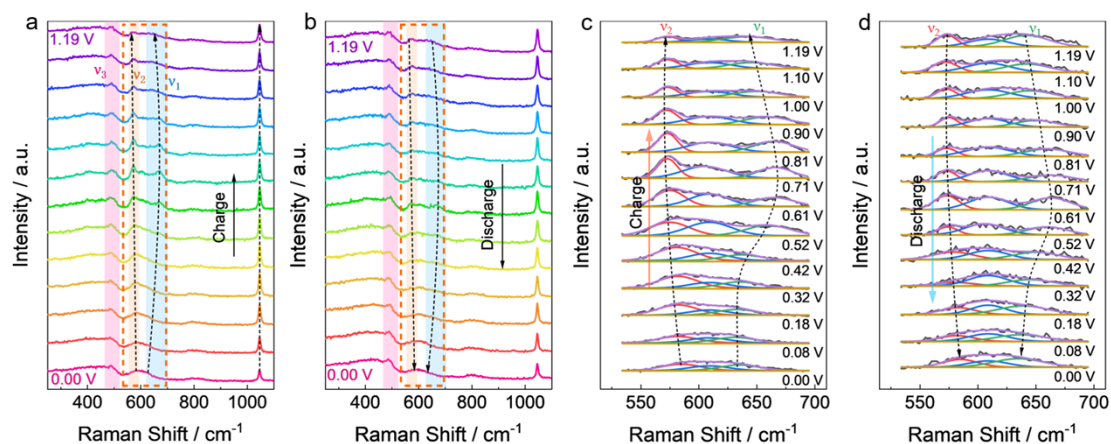


Figure S17. (a-b) *Operando* Raman spectra of Rec-Mg-MnO₂ at different charged and discharged states. (c-d) The corresponding *operando* Raman spectra in the range of 530 cm⁻¹ to 695 cm⁻¹.

Supplementary Note 6

We also studied the influence of cation concentration. The electrode activated and tested in 0.5 M $\text{Mg}(\text{NO}_3)_2$ aqueous electrolyte was denoted as Rec-Mg-MnO₂-0.5 (Fig. S18a-c). Compared to CV and GCD curves of Rec-Mg-MnO₂ in 1 M $\text{Mg}(\text{NO}_3)_2$ (Rec-Mg-MnO₂-1), Rec-Mg-MnO₂-0.5 displays a smaller integrated CV area and shorter discharge time (Fig. S18d and e), representing a compromised performance for Rec-Mg-MnO₂-0.5. Therefore, refining both the cation concentration and type is highly desired for the design of electrochemical reaction systems, which is expected to present novel opportunities for enhanced energy storage.

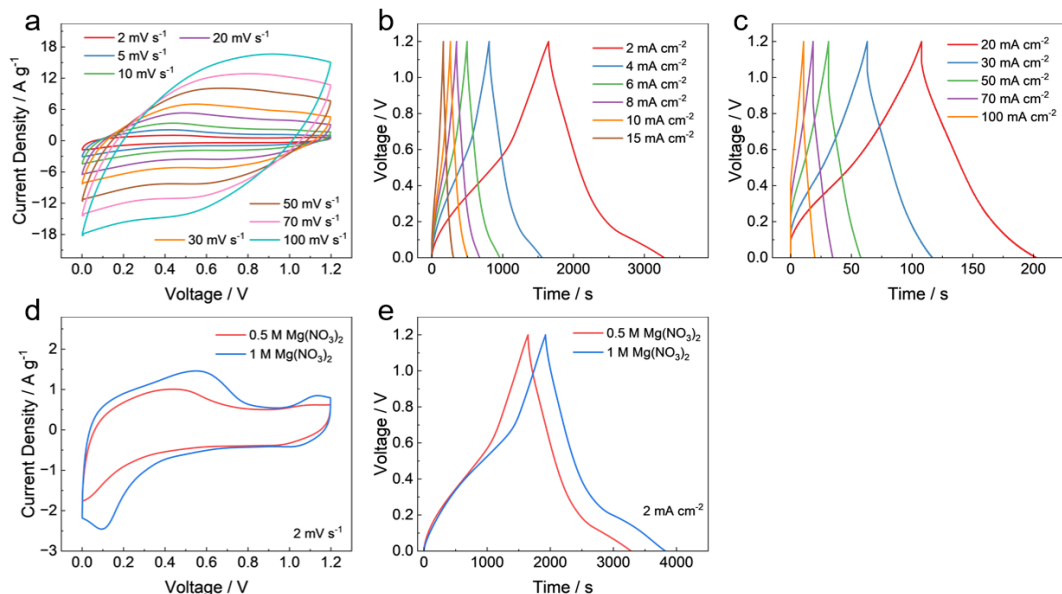


Figure S18. (a-c) Electrochemical performance of Rec-Mg-MnO₂ in 0.5 M Mg(NO₃)₂ electrolyte. (a) CV curves at different scan rates. (b-c) GCD profiles at different current densities. (d-e) The comparison of electrochemical behaviour for Rec-Mg-MnO₂ electrode in 0.5 M Mg(NO₃)₂ and 1 M Mg(NO₃)₂ electrolytes. (d) CV curves at 2 mV s⁻¹. (e) GCD profiles at 2 mA cm⁻².

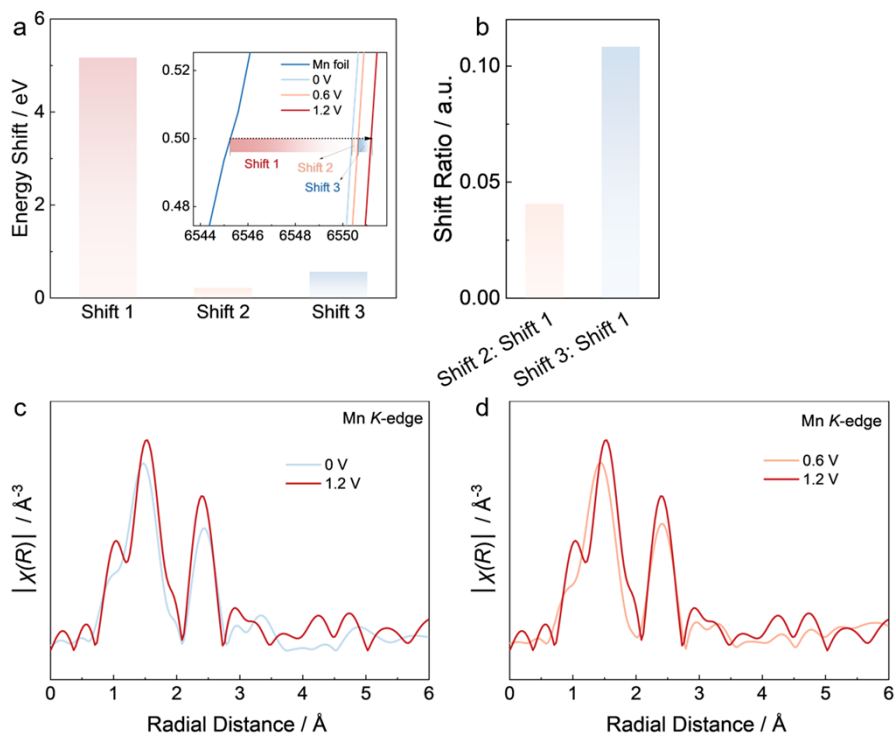


Figure S19. (a) Energy shifts in Mn K-edge XANES spectra of Rec-Mg-MnO₂ at

different charged states and Mn foil with the normalized intensity of 0.5, typically, the shift from Mn foil to 0 V (Shift 1), the shift from 0 V to 0.6 V (Shift 2), and the shift from 0.6 V to 1.2 V (Shift 3). (b) The corresponding ratios between the typical shift values. (c-d) Comparison of the k^3 -weight Fourier transformation (c) between 0 V and 1.2 V, as well as (d) between 0.6 V and 1.2 V.

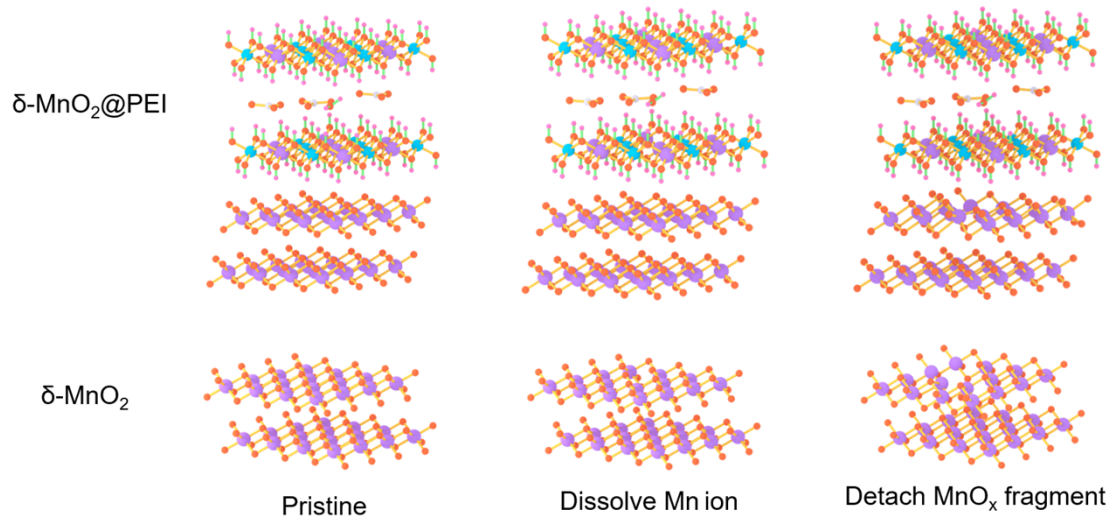


Figure S20. Schematic illustration of dissolution process of Mn ions and the subsequently detachment process of active MnO_x fragment.

Supplementary Note 7

The Mn-O bond length was calculated to further investigate the impact of PEI on the structure stability. As shown in Fig. S21 and Table S1, the Mn-O distance was strongly stretched along the O5-Mn-O6 direction, leading serious structural distortion in MnO₂. However, this elongation is depressed in some degree for MnO₂ with the presence of PEI, indicative of the suppressed Jahn-Teller distortion and strong structure stability towards a better long-cycling performance.

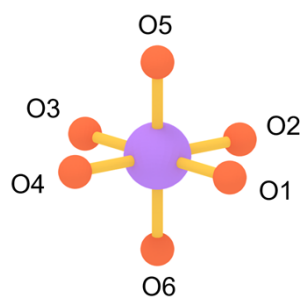


Figure S21. Schematic illustration of Mn-O bonds in the $[\text{MnO}_6]$ octahedron.

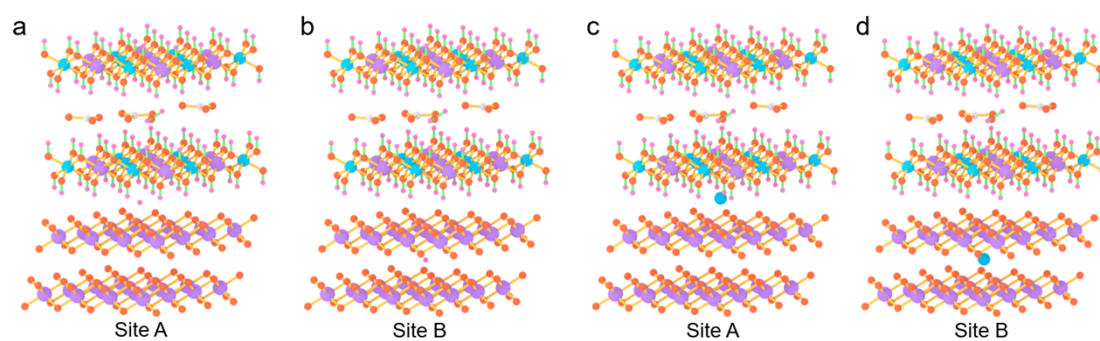


Figure S22. (a-b) The simulated H^+ adsorption models at (a) site A and (b) site B of the $\text{MnO}_2@\text{PEI}$ structure. (c-d) The simulated Mg^{2+} adsorption models at (c) site A and (d) site B of the $\text{MnO}_2@\text{PEI}$ structure.

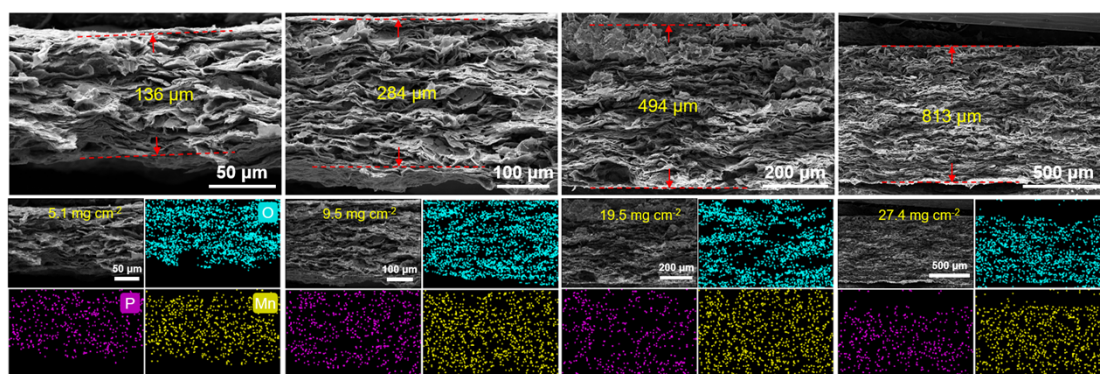


Figure S23. Cross-section SEM images and the corresponding elemental mapping images of the $\text{P-Mn}_3\text{O}_4@\text{C}$ electrodes with different mass loadings.

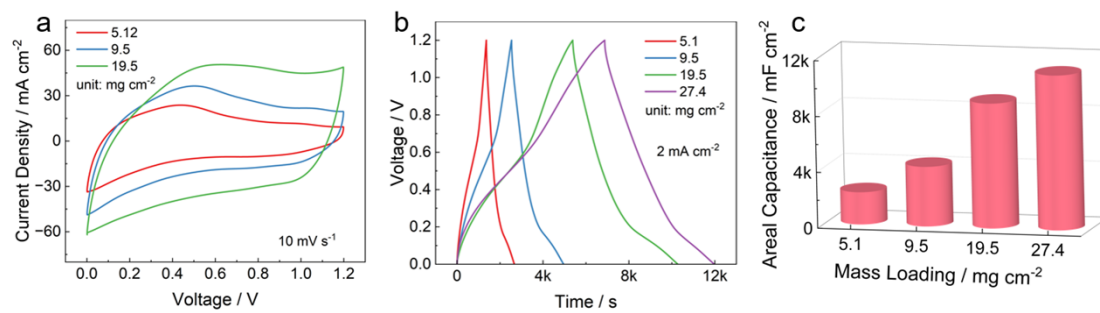


Figure S24. Electrochemical performances of Rec-Mg-MnO₂ electrodes with different mass loadings. (a) CV curves at 10 mV s⁻¹, (b) GCD profiles, and (c) corresponding areal capacitance at 2 mA cm⁻².

Supporting Table

Table S1. The Mn-O bond length values for the pure δ -MnO₂ and MnO₂@PEI.

Bond	Bond length	
	Pure δ -MnO ₂	MnO ₂ @PEI
Mn-O1	1.9182 Å	1.9209 Å
Mn-O2	1.9181 Å	1.9206 Å
Mn-O3	1.9182 Å	1.9209 Å
Mn-O4	1.9182 Å	1.9206 Å
Mn-O5	1.9675 Å	1.9441 Å
Mn-O6	1.9675 Å	1.9441 Å

Table S2. A comparison of specific capacitance, mass-loading and cycle performance for the tailored Rec-Mg-MnO₂ electrode and related results in literature.

Electrode Materials	Electrolyte	Specific Capacitance	Mass-Loading	Cycle Performance	Ref.
Rec-Mg-MnO ₂	1 M Mg(NO ₃) ₂	495 F g ⁻¹	6.4 mg cm ⁻²	92% (25000 cycles)	<i>This work</i>
		405 F g ⁻¹	27.4 mg cm ⁻²	/	
O _v -MnO ₂ -30	1 M Na ₂ SO ₄	403 F g ⁻¹	11.9 mg cm ⁻²	95% (10000 cycles)	<i>Energy Environ. Sci.</i> , 2024, 17, 3384-3395
MnO ₂ /nitrogen-doped carbon	1 M Na ₂ SO ₄	480 F g ⁻¹	19.7 mg cm ⁻²	90% (10000 cycles)	<i>Adv. Funct. Mater.</i> , 2021, 31, 2009632
NMO _x	1 M Na ₂ SO ₄	476 F g ⁻¹	/	96% (10000 cycles)	<i>Adv. Funct. Mater.</i> , 2022, 32, 2206539
MnO ₂ -TEA	1 M Na ₂ SO ₄	418 F g ⁻¹	2 mg cm ⁻²	85.5% (10000 cycles)	<i>Adv. Energy Mater.</i> , 2021, 11, 2101412
AK-MnO ₂	1 M Na ₂ SO ₄	356 F g ⁻¹	0.9 mg cm ⁻²	84% (5000 cycles)	<i>Matter</i> , 2021, 4, 2902-2918
Na _{0.5} MnO ₂	1 M Na ₂ SO ₄	366 F g ⁻¹	1-2 mg cm ⁻²	96% (10000 cycles)	<i>Adv. Mater.</i> , 2017, 29, 1700804

Ni-MnO ₂	1 M Na ₂ SO ₄	327 F g ⁻¹	/	91% (11000 cycles)	<i>Nano Energy</i> , 2022, 99, 107391
MnO ₂ -Pc	1 M Na ₂ SO ₄	338 F g ⁻¹	/	84% (10000 cycles)	<i>Adv. Energy Mater.</i> , 2023, 13, 2300384
β-MnO ₂ / birnessite	1 M Na ₂ SO ₄	306 F g ⁻¹	2-3 mg cm ⁻²	92% (3000 cycles)	<i>ACS Nano</i> , 2018, 12, 1033-1042
0.8V-MnO ₂	0.5 M Na ₂ SO ₄	190 F g ⁻¹	2 mg cm ⁻²	91% (5000 cycles)	<i>Adv. Funct. Mater.</i> , 2021, 31, 2102693
Mn ₂ O ₃ @TiO ₂ @MXene//AC	0.5 M MgSO ₄	292 F g ⁻¹	1.3 mg cm ⁻²	~100% (2400 cycles)	<i>Small Struct.</i> , 2024, 5, 2300371
MnO ₂ -60	1 M Na ₂ SO ₄	304 F g ⁻¹	10.0 mg cm ⁻²	108% (2000 cycles)	<i>ACS Nano</i> , 2018, 12, 3557-3567

References

- 1 W. Guo, C. Yu, C. T. Zhao, Z. Wang, S. F. Li, J. H. Yu, X. Y. Tan, Y. Y. Xie, L. Yang, H. L. Huang, R. Fu and J. S. Qiu, *Energy Storage Mater.*, 2020, **31**, 172-180.
- 2 F. Li, J. Qu, Y. Li, J. H. Wang, M. S. Zhu, L. X. Liu, J. Ge, S. K. Duan, T. M. Li, V. K. Bandari, M. Huang, F. Zhu and O. G. Schmidt, *Adv. Sci.*, 2020, **7**, 2001561.
- 3 G. Kresse and J. Furthmuller, *Phys. Rev. B*, 1996, **54**, 11169-11186.
- 4 G. Kresse and D. Joubert, *Phys. Rev. B*, 1999, **59**, 1758-1775.
- 5 J. P. Perdew, K. Burke and M. Ernzerhof, *Phys. Rev. Lett.*, 1996, **77**, 3865-3868.
- 6 S. Grimme, J. Antony, S. Ehrlich and H. Krieg, *J. Chem. Phys.*, 2010, **132**, 154104.
- 7 P. E. Blochl, *Phys. Rev. B*, 1994, **50**, 17953-17979.
- 8 G. Henkelman, B. P. Uberuaga and H. Jonsson, *J. Chem. Phys.*, 2000, **113**, 9901-9904.
- 9 J. Deng, D. H. Deng and X. H. Bao, *Adv. Mater.*, 2017, **29**, 1606967.
- 10 L. Yu, D. H. Deng and X. H. Bao, *Angew. Chem. Int. Ed.*, 2020, **59**, 15294-15297.
- 11 Y. P. Zhu, J. Yin, A. H. Emwas, O. F. Mohammed and H. N. Alshareef, *Adv. Funct. Mater.*, 2021, **31**, 2107523.
- 12 M. Huang, X. P. Wang, J. J. Wang, J. S. Meng, X. Liu, Q. He, L. S. Geng, Q. Y.

- An, J. L. Yang and L. Q. Mai, *Angew. Chem. Int. Ed.*, 2023, **62**, e202308961.
- 13 K. W. Leong, W. D. Pan, X. P. Yi, S. J. Luo, X. L. Zhao, Y. G. Zhang, Y. F. Wang, J. J. Mao, Y. Chen, J. Xuan, H. Z. Wang and D. Y. C. Leung, *Sci. Adv.*, 2023, **9**, eadh1181.
- 14 Y. Song, Q. Pan, H. Z. Lv, D. Yang, Z. M. Qin, M. Y. Zhang, X. Q. Sun and X. X. Liu, *Angew. Chem. Int. Ed.*, 2021, **60**, 5718-5722.
- 15 K. Li, X. H. Wang, X. F. Wang, M. Y. Liang, V. Nicolosi, Y. X. Xu and Y. Gogotsi, *Nano Energy*, 2020, **75**, 104971.
- 16 W. Guo, C. Dun, C. Yu, X. Song, F. Yang, W. Kuang, Y. Xie, S. Li, Z. Wang, J. Yu, G. Fu, J. Guo, M. A. Marcus, J. J. Urban, Q. Zhang and J. Qiu, *Nat. Commun.*, 2022, **13**, 1409.
- 17 S. Liu, Y. Yin, D. X. Ni, K. S. Hui, K. N. Hui, S. Lee, C. Y. Ouyang and S. C. Jun, *Energy Storage Mater.*, 2019, **19**, 186-196.
- 18 D. X. Ji, L. Fan, L. Tao, Y. J. Sun, M. G. Li, G. R. Yang, T. Q. Tran, S. Ramakrishna and S. J. Guo, *Angew. Chem. Int. Ed.*, 2019, **58**, 13840-13844.
- 19 Q. Chen, J. L. Jin, M. D. Song, X. Y. Zhang, H. Li, J. L. Zhang, G. Y. Hou, Y. P. Tang, L. Q. Mai and L. Zhou, *Adv. Mater.*, 2022, **34**, 2107992.
- 20 Z. H. Huang, Y. Song, D. Y. Feng, Z. Sun, X. Q. Sun and X. X. Liu, *ACS Nano*, 2018, **12**, 3557-3567.
- 21 D. Yang, Y. Song, M. Y. Zhang, Z. M. Qin, J. Liu and X. X. Liu, *Angew. Chem. Int. Ed.*, 2022, **61**, e202207711.
- 22 J. M. Cerrato, M. F. Hochella, W. R. Knocke, A. M. Dietrich and T. F. Cromer, *Environ. Sci. Technol.*, 2010, **44**, 5881-5886.
- 23 C. Zhang, X. Zhan, T. Al-Zoubi, Y. L. Ma, P. C. Shih, F. F. Wang, W. X. Chen, S. Pidaparthi, R. M. Stephens, Q. Chen, J. M. Zuo and H. Yang, *Nano Energy*, 2022, **102**, 107696.
- 24 W. L. Zhao, F. H. Xu, L. Q. Liu, M. Liu and B. C. Weng, *Adv. Mater.*, 2023, **35**, 2308060.
- 25 Y. Zuo, T. F. Meng, H. Tian, L. Ling, H. L. Zhang, H. Zhang, X. H. Sun and S. Cai, *ACS Nano*, 2023, **17**, 5600-5608.

- 26 D. Yang, Y. Song, M. Y. Zhang, Z. M. Qin, R. Dong, C. C. Li and X. X. Liu, *Adv. Funct. Mater.*, 2021, **31**, 2100477.
- 27 S. Rubio, Z. T. Liang, X. S. Liu, P. Lavela, J. L. Tirado, R. Stoyanova, E. Zhecheva, R. Liu, W. H. Zuo, Y. Yang, C. Pérez-Vicente and G. F. Ortiz, *Energy Storage Mater.*, 2021, **38**, 462-472.